Frolova and Derhachov *Nanoscale Research Letters* (2017) 12:505
DOI 10.1186/s11671-017-2268-5

Nanoscale Research Letters

NANO EXPRESS Open Access

The Effect of Contact Non-equilibrium Plasma on Structural and Magnetic Properties of $Mn_XFe_{3-X}O_4$ Spinels

L.A. Frolova[1*] and M. P. Derhachov[2]

Abstract

Nano-sized manganese ferrites $Mn_xFe_{3-x}O_4$ (x = 0–1.3) were prepared using contact non-equilibrium plasma (CNP) in two different pH (11.5 and 12.5). The influence of synthesis conditions (e.g., cation ratio and initial pH) on phase composition, crystallite size, and magnetic properties were investigated employing X-ray diffraction (XRD), differential thermal analysis (DTA), Fourier transform infrared (FTIR), scanning electron microscopy (SEM), transmission electron microscopy (TEM), and magnetic measurement techniques. The formation of monodispersed faceted ferrite particles at x = 0–0.8 was shown. The FTIR spectra revealed reflection in region 1200–1700 cm^{-1} caused by the presence of water adsorbed on the surface of $Fe_{3-x}Mn_xO_4$ micro-granules or embedded into their crystal lattice. The most sensitivity of reflection spectra to the composition changes takes place within a 400–1200 cm^{-1} range, typical to the stretching vibrations of Fe(Mn)–O (up to 700 cm^{-1}), Fe(Mn)–OH, and Fe(Mn)–OH_2 bonds (over 700 cm^{-1}). The XRD results showed that the nanocrystalline $Mn_xFe_{3-x}O_4$ ($0 < x < 1.0$) had cubic spinel crystal structure with average crystallite size 48–49 A. The decrease of crystalline size with the x increase was also observed.

Keywords: $MnFe_2O_4$ spinel, Preparation, Combustion, Chemical precipitation, Characterization, CNP

Background

The ability of nanodispersive spinels with polyvalent metals to form a number of solid solutions and compounds gives unlimited possibilities to control technological properties of spinel compounds. For a long time, great attention of many researchers has been paid to the investigations of manganese ferrites (Fe_3O_4 – Mn_3O_4 system) because of their wide application in industry. They are widely used in microwave ovens and magnetic storage devices, as well as highly active catalysts in producing hydrogen via methane dehydrogenation into ethylene or acetylene, adsorbents [1–6].

The synthesis of manganese ferrite spinel is technologically complex. Presently, there are few methods for the synthesis of manganese ferrite particles, such as ceramic [7], coprecipitation [8–12], hydrothermal method [13], reverse micelle [14, 15], sol-gel [16], combustion method [17], mechanosynthesis [18–20], high-energy technologies [21, 22], and mechanical doping [23, 24]. Hydrophase methods allow regulating composition, crystallinity, and particle morphology.

Such methods have been studied by many researchers and are successfully applied for synthesis of ferrites [9, 25, 26] with particle size of 30–50 nm at 50–150 °C, which is significantly lower than for ceramic technology. Hydrophase methods, as a rule, include several stages: the first—deposition, the second—directly ferrite synthesis, carried out due to oxidation, aging, etc. The methods for initiation of the second main stage of ferrite synthesis using ultrasound treatment, microwave influence, ultraviolet, and various discharges [27–29] have been used recently. During the treatment of solutions with discharge of CNP, a complicated complex of chemical reactions involving radical particles and free electrons occurs. The main products of such interactions are oxygen, hydrogen, and hydrogen peroxide. Oxidative activity of plasmochemically "activated" solutions can be used for synthesis of complex oxide compounds.

The emission spectrum [30–32] has shown that the main contributions to the emission spectrum of the water

* Correspondence: frolova_l.a@mail.ru
[1]Ukrainian State University of Chemical Technology, Gagarin Ave., 8, Dnipropetrovsk 49005, Ukraine
Full list of author information is available at the end of the article

vapor plasma are OH, atomic hydrogen, and the oxygen radical. In the case of the bubble mode, when the streamers fill the entire bubble, a significant emission from the nitrogen second positive system and the nitrogen ion (first negative system). The discharge operates in two different modes. For small conductivities of the liquid, the discharge is a direct liquid streamer discharge (liquid mode). This mode is similar to the typical so-called corona discharges in water. For conductivities above typically 45 μS cm^{-1} a large vapor bubble is formed. In the bubble mode, the streamers are located at the bubble–liquid interface. The hydrogen peroxide formation efficiency is dependent on power with a maximum for intermediate powers. The hydrogen peroxide formation efficiency is significantly smaller in the bubble mode than in the liquid mode. In the work [33], the kinetic parameters of electrons for the dielectric barrier discharge with a liquid electrode at atmospheric pressure have been estimated. Thus, we may suppose that the CNP will possess chemical activity with respect to its application in realization of the different oxidative-reductive processes.

Our preliminary studies of plasma treatment of solutions have shown that the composition of synthesized oxidizer solution depends on a wide range of factors [29]. The use of CNP guarantees high degree of homogeneity in component distribution both in the initial solution and in the product formed during oxidation, which stimulates effective interaction between them with formation of ferrites with homogeneous structure and composition.

The aim of the work is to study the possibility of obtaining nano-sized $Mn_XFe_{3-X}O_4$ spinel from aqueous solutions using contact non-equilibrium plasma. Since ferrites are solid solutions, it is important to establish the degree of their structural and concentration homogeneity under the selected synthesis conditions. The experimental method consisted in comparison of ferrospinel obtained from manganese and iron sulfates at different cation ratio.

Such comparative research of the samples allow establishing the influence of the chemical composition of the initial solution and the synthesis conditions on the structural-phase state of the compounds prepared using CNP treatment.

Methods

For the synthesis of manganese ferrite, the authors have used aqueous solutions of $FeSO_4{\cdot}7H_2O$, $MnSO_4{\cdot}5H_2O$, and aqueous solution of NaOH was used as a precipitant. We used 0.5 M solutions of iron and manganese salts. All the chemicals and solvents employed for the synthesis were of analytical grade and used as received without further purification. Deionized water was used as solvent in whole procedure.

Preliminary studies [25] showed that at pH < 11 nonmagnetic oxides and oxyhydroxides were formed, so two sets of samples were prepared. The first set at initial pH = 11.5 and the second at 12.5. The coprecipitated compounds were prepared by pouring at continuous stirring of corresponding mixture of sulfate solutions with necessary cation ratio. The further treatment was carried out using CNP.

The treatment was conducted in a cylindrical reactor with inner diameter of 45 mm and height of 85 mm. The reaction mixture was cooled by the continuous circulation of cold water in the outer jacket. One of stainless steel electrodes (diameter 4 mm) was located in the lower part of the reactor, and the other (diameter 2.4 mm) was located 10 mm above the surface of the solution. The initial voltage was delivered to the step-up transformer. The ac current from the secondary coil was delivered to the bridge rectifier and then, now pulsating voltage, was delivered via a ballast resistor to the reactor electrodes. The igniting unit was additionally connected to the anode. This unit formed pulses with amplitude of up to 15 kV at a width of 1.5 ms. The pulses were strictly synchronized with the phase of the pulsating voltage. At the instant when the igniting pulse was formed, there was a breakdown between the reactor electrodes in the vacuum space created by rarefaction to 0.06–0.08 MPa. The resistance sharply dropped, and an anode current started to flow thereby creating a discharge. The discharge burning voltage remained nearly unchanged at 750–900 V. The current in the discharge gap was determined by the plasma resistance and the voltage applied to the system formed by the plasma discharge and the ballast controller. The voltage was controlled by the phase method principle, i.e., the average anode voltage applied to the reactor depended on the phase of the pulsating voltage at the anode and on the instant at which an ignition pulse was delivered.

The plasma appeared at the ignition instant and was extinguished when the anode voltage pulsations terminated (Fig. 1). The repetition frequency of the process was 100 Hz. The discharge current was controlled by changing the instant of ignition relative to the phase of anode voltage pulsations with a synchronizing device. The duration of plasma treatment varied from 10 to 40 min. All precipitates were washed until negative reaction on sulfate-ion. The washed and filtered precipitates were dried at 150 °C. Relative magnetic properties (of saturation magnetization I_S (emu^2/g), coercive force Hc (Oe)) were evaluated by magnetometer [29].

The concentration of Mn^{2+} in the samples obtained was determined complexometrically. The concentration of iron was determined using permanganate and bichromate methods. In order to monitor the reaction process, the reactor was equipped with an electrode system. The $[Fe^{2+}]/[Mn^{2+}]$ ratio in $Mn_xFe_{3-x}O_4$ compound was calculated according to formula:

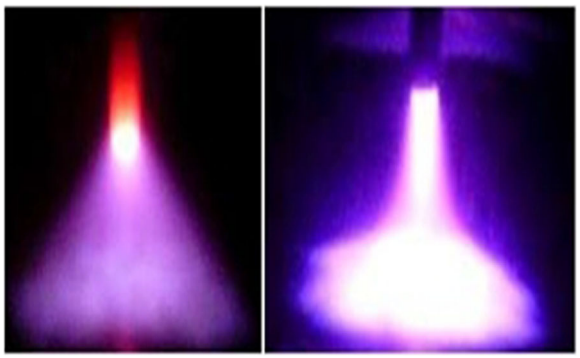

Fig. 1 The pillar of contact non-equilibrium plasma between the electrode in the gas phase and the surface of the liquid

$$\frac{C_{Mn}}{C_{Fe}} = \frac{x}{3-x}$$

and values were equal of x = 0; 0.2, 0.4, 0.6, 0.8, 0.9, 1, 1.1, 1.2, and 1.3 were chosen. Fourier transform infrared reflection spectra of manganese ferrites $Mn_xFe_{3-x}O_4$ (x = 0.0, 0.2, 0.4, 0.6, 0.8, 0.9, 1.0, 1.1, 1.2, 1.3) were measured within a 400–4000 cm^{-1} range by employing a Fourier transform infrared (FTIR) spectrometer Nicolet iS10. To study the transformations occurring upon heating of obtained powders, we used differential thermal analysis (DTA) and differential thermogravimetric analysis (DTG). DTA, mass loss TG, and mass loss rate DTG curves were recorded on Derivatograph Q-1500D (F. Paulik, J. Paulik, and L. Erdey). The temperature was varied in range 20–1000 °C at heating rate of 10°/min. γ-Al_2O_3 was used as a reference. The mass of each sample was 200 mg. The morphology of the ferrite powders and the particle size were studied using scanning electron microscopy. The phase composition (XRD) and the structure of the ferrite samples were studied using X-ray diffractometer DRON-2 in monochromatized Co-K_α radiation. The crystallite size and the degree of microstrains were calculated using approximation method. The size and the shape of the particles were determined using electron Microscope "Jem 1010" (JEOL) at working value voltage of 200 kV. Scanning electron microscopy with X-ray microanalysis was carried out using REMMA-102 (SELMI, Ukraine).

Results and Discussion

Properties of magnetic materials based on manganese ferrites depend on their structural and phase state. The synthesis of such ferrites call for preparation of single-phase product with spinel structure not having residual iron oxide or other phases, which are intermediate products of ferrite formation from oxides. On par with phase composition, the magnetic properties are significantly influenced by oxidation of iron and manganese cations, and character of their location in site of spinel crystal lattice. It is known that divalent cations (Zn^{2+}, Mn^{2+}) are mostly located in tetrahedral positions and trivalent (Fe^{3+})—in octahedral positions of spinel crystal lattice. According to Néel relaxation theory, such arrangement provides maximum value of material magnetization. During preparation of ferrites, oxidation of Mn^{2+} to Mn^{3+} is possible, which can be accompanied by reduction of Fe^{3+} to Fe^{2+} and rearrangement of cations in sublattices, with partial transfer of Fe^{2+} into tetrahedral and Mn^{3+}—into octahedral nodes of crystal lattice, which negatively impacts magnetic properties of ferrites. Oxidation of Mn^{2+} occurs at highest rate at 900–1000 °C, and optimal condition for sintering of manganese ferrites for ceramic technology—1000–1200 °C. The data available in various literature sources on discussion of magnetic structure and properties of manganese ferrites are contradictory, which is likely related to variation in arrangement of iron and manganese ions and their polyvalency. The data of the dependence of lattice parameter on the value of x in case of various technologies make it possible to assume the character of cation arrangement in the lattice.

The assessment results of prepared samples can be formulated as follows: all samples include chemically bound water in various amounts. In both sets, the highest water content is found in samples with x = 0.4, 1.1…1.3. The first set showed weak magnetic properties (Figs. 2 and 3), and so it was not considered in detail.

As can be seen from Fig. 1, there are some differences in saturation magnetization of both sets. The highest value for set 1 corresponds to ratio 1,1 $Mn_{1.0}Fe_{0.9}Mn_{0.1}O_4$. The highest value is achieved at pH = 12.5 and ratio of x = 0.8 ($Mn_{0.8}Fe_{0.2}Fe_2O_4$). This ratio is different from stoichiometric manganese ferrite.

By assessing saturation magnetization, it can be said that sample nos. 1, 2, 3, and 8 have lower values due to

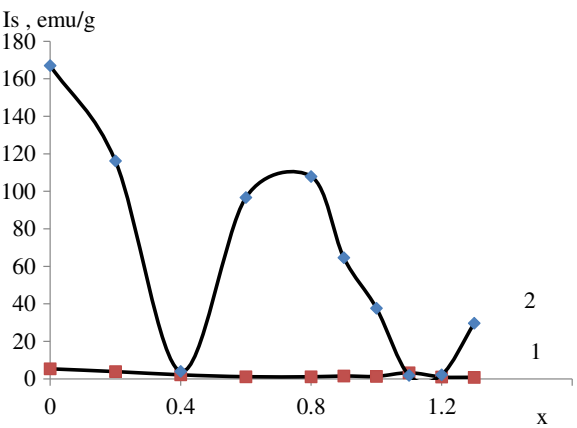

Fig. 2 Dependence of saturation magnetization on cation molar ratio at different pH: 1—pH = 11.5 and 2—pH = 12.5

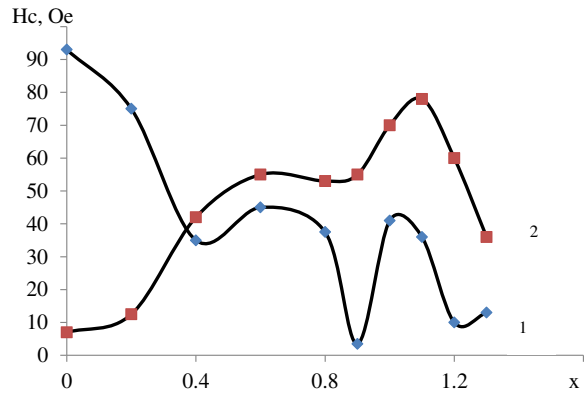

Fig. 3 Dependence of coercive force on cation molar ration at different pH: 1—pH = 11.5 and 2—pH = 12.5

their amorphous structure and presence of non-magnetic phases.

Figure 4 shows XRD patterns of samples from the second set. The XRD patterns may be divided into two categories—first samples 6–10 that have monophase crystal structure corresponding to spinel phase ferrite (JCPDS 10-0467). Relatively sharp and intense lines of spinel phase ferrites can be observed on XRD patterns of the samples. The lines related to oxide phases of Fe_2O_3 and MnO_x are absent on XRD patterns (Fig. 4).

The second set has less crystalline with few phases present. On XRD patterns of the samples, prepared with higher manganese content, the lines are slightly broadened, which may indicate changes in its structure in comparison with the stoichiometric sample. Presence of other phases in case of higher manganese content was found using XRD method. The broad peaks can be observed on XRD patterns, which can be indexed as (311) of ferrite's spinel phase (JCPDS 74-2403). In the region of angles corresponding to the highest intensity lines for Fe_3O_4 and Mn_3O_4, a halo of low intensity is observed, which can indicate the presence of these oxides in the samples. There is a clear correlation between the magnetic characteristics and the degree of crystallinity and homogeneity of the product.

Taking into account that Mn^{2+} cations are the largest of all, it could be assumed that as the value of x increases, it is possible to increase the lattice parameter. The analysis of XRD patterns (Fig. 5) shows that the parameter of crystal lattice a = 8.4196 A (for stoichiometric tetragonal manganese ferrite $MnFe_2O_4$ a = 8.51 A). Noticeably smaller value of lattice parameter can be explained with formation of manganese ferrite at pH = 12.5 following magnetite formation mechanism. Upon oxidation of Mn^{2+}:

$3Mn^{2+} \rightarrow 2Mn^{3+} + \square$

vacancies are formed, which facilitate reduction of lattice parameters. Magnetite is formed in the second set, and gradual substitution of iron cations with manganese cations leads to reduction of magnetic properties to ratio 0.4 (the first peak) following 1-1,1, corresponding to stoichiometric manganese ferrite. Analysis of Figs. 2 and 3 makes it possible to establish that the formation of compounds in the second set occurs according to the maghemite formation mechanism.

As stated in Table 1, ferrite $Mn_XFe_{3-X}O_4$ was obtained in the nanorange. The average crystallite size of nanoparticles $Mn_XFe_{3-X}O_4$ were ranged from 5 to 8 nm and reached a maximum at x = 0. The calculated $Mn_XFe_{3-X}O_4$ crystalline size exceeded ferrite crystallite size in TEM image in four times due to aggregation of nanoparticles.

Also, Table 1 shows the variation of Curie temperature, lattice parameter with ratio x in $FeMn_{2-x}O_4$. Curie temperature decreases as cations manganese content increases. As it can be known, Curie temperature is mainly determined by the strongest super exchange interaction in ferrites. The factors decreasing this interaction lead to a decrease in Curie temperature. With an increase in the manganese content, the lattice parameter increases (Table 1). This leads to an increase in ionic distances as well as decrease in Curie temperature.

The present assumption requires additional study. Analysis of derivatography patterns indicates on formation of manganese ferrite in sample nos. 4 and 5 and isomorphism of properties for samples 5–10 (Fig. 6). The compounds of various composition are formed in samples 1–5. The lowest mass losses are also observed for stoichiometric compositions. The first regions of derivatography patterns demonstrate various endo- and exothermic effects corresponding to oxidation of manganese and iron cations. High temperature region corresponds to rearrangement of crystal lattice (endo-effects without changing the mass).

DTG curves demonstrate that for all compositions the main mass loss corresponds to the loss of free water at 100 °C and bound at 160 °C. For composition 4, corresponding to stoichiometric ferrite, exothermic peaks are observed, which correspond to oxidation of manganese cation to various oxidation states. In the work [34], the authors have presented the following set of reaction occurring at various temperatures.

1. $3\ Fe^{2+} \rightarrow 2Fe^{3+} + \square$ temperature 280 °C
2. $4\ Mn^{3+} \rightarrow 3Mn^{4+} + \square$ temperature 330 °C
3. $3\ Mn^{2+} \rightarrow 2Mn^{3+} + \square$ temperature 360 °C
4. $3Mn^{4+} + \square \rightarrow 4Mn^{3+}$ temperature 420 °C
5. $2Mn^{2+} \rightarrow Mn^{3+}$ temperature 600 °C

Upon heating to 450–500 °C a structure of γ-Fe_2O_3 type is formed.

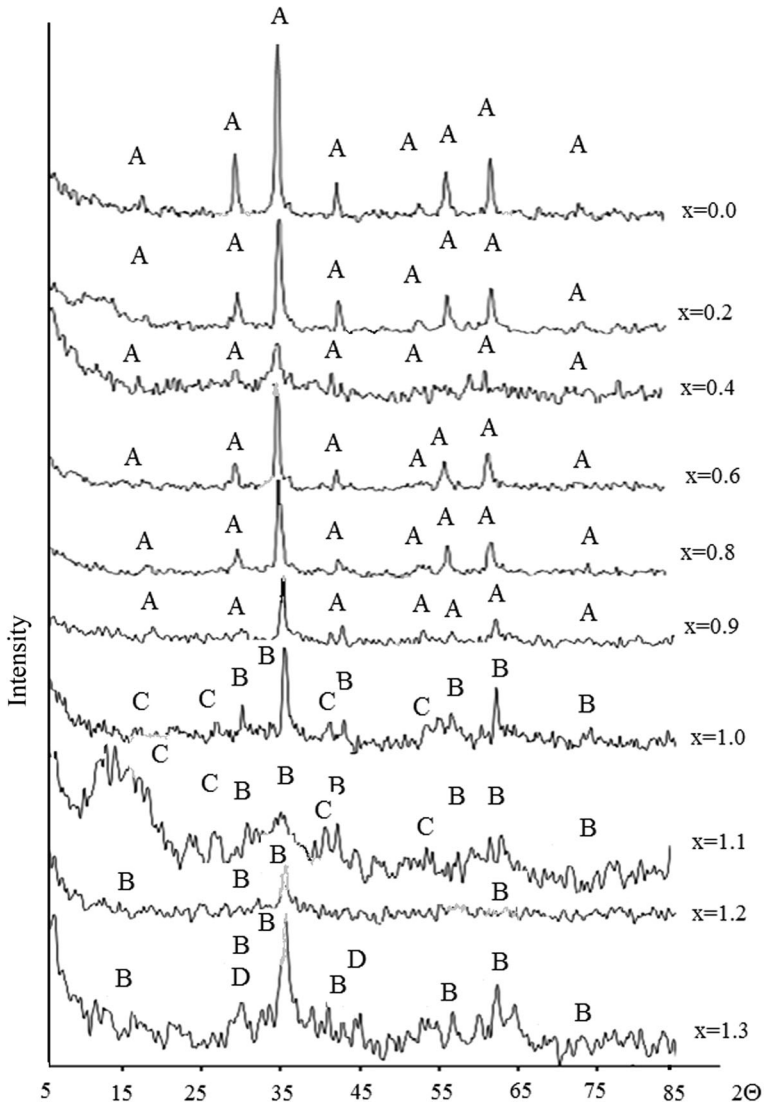

Fig. 4 XRD patterns of ferrite obtained at different ratios of components (Table 1): A—Fe_3O_4, B—$MnFe_2O_4$, C—Mn_3O_4, and D—β-MnO_2

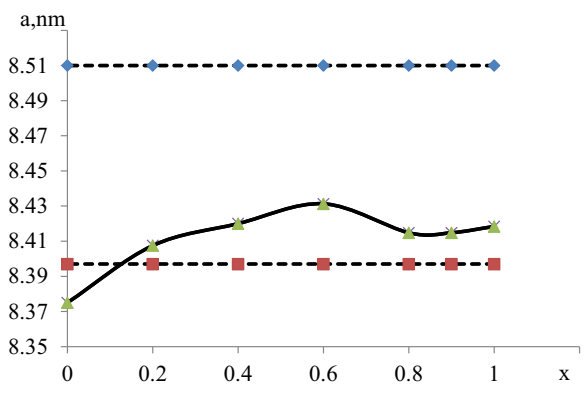

Fig. 5 Dependence of crystal lattice parameter on cation ratio *x*

It can be assumed, that peaks at 600 °C correspond to oxidation and reduction of iron and manganese cations. Further oxidation is accompanied with transition from cubic to rhombohedral lattice, in which all cations are trivalent. The formation of α-Fe_2O_3 and α-Mn_2O_3 occurs in range from 600 to 1000 °C. XRD analysis of products obtained after heating to 1000 °C indicates the presence of magnetic phase of rhombohedral manganese ferrite for the samples with stoichiometric ratio of iron and manganese formed from iron and manganese oxides.

In addition, upon heading samples 1–10 to 1000 °C (Table 1), the formation of complex iron and manganese oxide occurs via similar mechanism. The formed compounds have similar peaks regardless of the initial composition. This is related to rhombohedral structure,

Table 1 Dependence of the main characteristics of products on composition

Sample number	*x*	Composition	a, A	Crystallite size, A	T_C, °C	Mass loss, %	Literature value a, A
1	1.3	$Mn_{1.3}Fe_{1.7}O_4$	Amorphous		315	11.5	
2	1.2	$Mn_{1.2}Fe_{1.8}O_4$	Amorphous		315	19.6	
3	1.1	$Mn_{1.1}Fe_{1.9}O_4$	Amorphous		305	16.4	
4	1	$MnFe_2O_4$	8.4184	48.8	320	13.4	8.51
5	0.9	$Mn_{0.9}Fe_{2.1}O_4$	8.4148	52.3	280	6.7	
6	0.8	$Mn_{0.8}Fe_{2.2}O_4$	8.4148	60.9	315	7.2	
7	0.6	$Mn_{0.6}Fe_{2.4}O_4$	8.4313	66.1	315	5.3	
8	0.4	$Mn_{0.4}Fe_{2.6}O_4$	Amorphous		320	15.4	
9	0.2	$Mn_{0.2}Fe_{2.8}O_4$	8.4075	66.3	580	6.2	
10	0	Fe_3O_4	8.3750	72.3	520	0	8.397

in which all cations are trivalent. Since hematite and hausmannite have similar structure, all XRD patterns have similar character.

According to TEM results, all samples synthesized using CNP method are composed of particle with regular faceted shape, with size ranging from 50 to 100 nm (Fig. 7). The product is monodisperse with average particle size 70–80 nm. The observed faceted particles are polycrystalline. Data acquired using SEM confirm that large ferrite particles are composed of very small primal particles and their size is not in agreement with values calculated using crystallite size (Table 1).

It is known from literature sources that in IR patterns of γ-Fe_2O_3 and Fe_3O_4, there are two main groups of characteristic lines allowing to judge intricate structural differences. These are lines related to vibrations of M–O and M–O–H bonds. Introduction of different metal ions into iron oxide, causing symmetry distortion of coordination environment of Fe^{3+} or changes in Fe–O bond constant, can lead to the splitting or shifting of characteristic lines of Fe–O bond vibrations. In case of homogeneous distribution of ion of different nature in crystal lattice of spinel structure, we can usually observe only shift of absorption line's maxima of characteristic oscillations.

Figure 8 shows IR spectra of the studied samples. The spectral distribution over 1200 cm^{-1} is quite independent of the sample composition (Fig. 8).

Reflection in this region is caused by the presence of water that is adsorbed on the surface of $Fe_{3-x}Mn_xO_4$ microgranules or embedded into their crystal lattice. The bands within a 1200–1700 cm^{-1} range are related to the bending H–O–H vibrations, and those within a 2400–3700 cm^{-1} range are due to the stretching vibrations of O–H bonds.

The most sensitivity of reflection spectra to the composition changes takes place within a 400–1200 cm^{-1} range, typical to the stretching vibrations of Fe(Mn)–O (up to 700 cm^{-1}), Fe(Mn)–OH and Fe(Mn)–OH_2 bonds (over 700 cm^{-1}). The spectral position of the most intensive band is varied with the *x* changing. Its most shift, from 715 cm^{-1} in the Fe_3O_4 spectrum (x = 0.0) up to 688 cm^{-1}, occurs for the sample with x = 0.8. The broadening of this band with the x increase is also observed (Fig. 8). Moreover, a new band at 445 cm^{-1} is confidently detected in the spectra of samples with x = 0.8 and 0.9. In addition to these features, we should mention a significant spectral redistribution in the x = 0.4 spectrum, as a result of the raising of 1039 cm^{-1} reflection band relatively to the band at 715 cm^{-1} in the x = 0.0 spectrum.

In accordance with crystallographic data, metal (Mn, Fe) ions may occupy positions with tetrahedral and octahedral oxygen neighboring [35]. The most probable positions for manganese ions at concentration of $x < 1.3$ are the tetrahedral positions corresponding to the Mn^{2+} charge state. The appearance of the octahedral-coordinated manganese ions with the same charge state is detected for the values of x within a 0.8–1.2 range. The filling of octahedral positions with Mn^{3+} ions starts at x = 1.0, and the part of them at x = 1.3 is no more than 23% from total quantity of manganese ions [35].

This is the reason to explain the changes observed in the x = 0.8 spectrum by starting the filling of octahedral positions with Mn^{2+} ions.

The raising of the 1039 cm^{-1} band in the x = 0.4 spectrum may be related to the structural variations in the metal (Mn, Fe) ions neighboring, that results in dipole momentum changing.

More detailed analysis is, unfortunately, complicated by essential overlapping of broadened bands that is typical for solid solutions containing tetrahedral and octahedral complexes with central atoms whose masses are close to each other.

Conclusions

In the present work, we have found a new route for the synthesis of ultrafine manganese ferrite of type

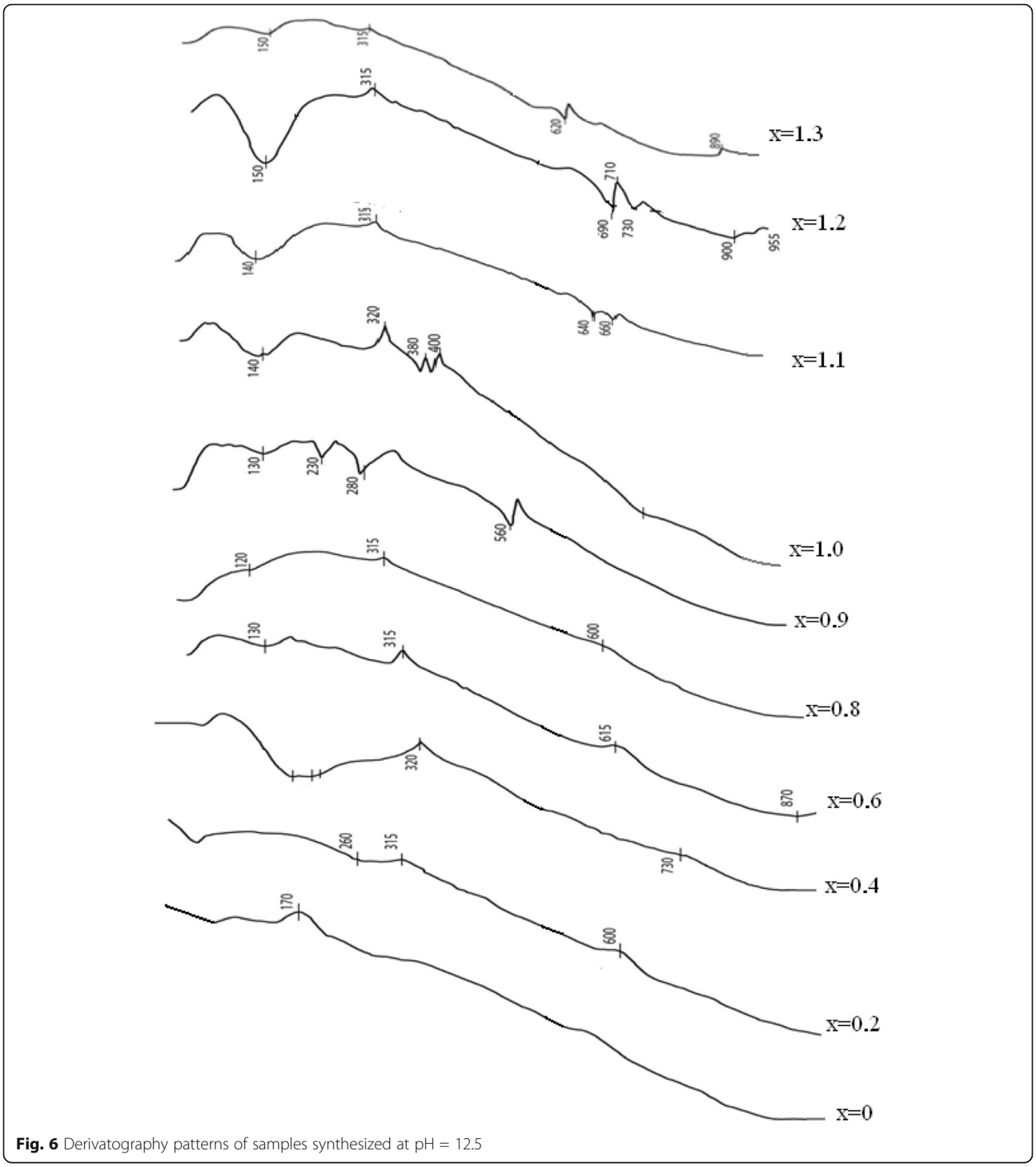

Fig. 6 Derivatography patterns of samples synthesized at pH = 12.5

$Mn_XFe_{3-X}O_4$ in a wide Mn^{2+} substitution range from x by coprecipitation with CNP treatment. Coprecipitation followed by CNP treatment is an effective method for the preparation of manganese ferrite powder. The magnetic properties of $Mn_XFe_{3-X}O_4$ samples were increased with increasing pH values. Ferritization process was effective only at pH = 12.5. The formation of compounds at pH = 11.5 occurs by the mechanism of the formation of maghemite. High magnetic properties exhibited nanodispersed ferrite obtained at pH = 12.5, x = 0.6–0.8. The average crystallite size ranged from 50 to 80 A. The nanodispersed ferrites had a faceted shape and uniform particles. XRD pattern indicates the single spinel phase nanocrystals with cubic spinel structure at $0 < x < 0.8$.

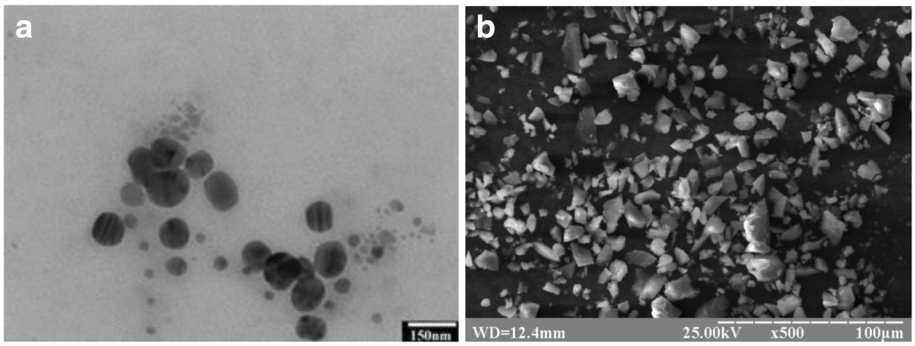

Fig. 7 TEM image (**a**) and SEM image (**b**) of sample no. 4 set 2

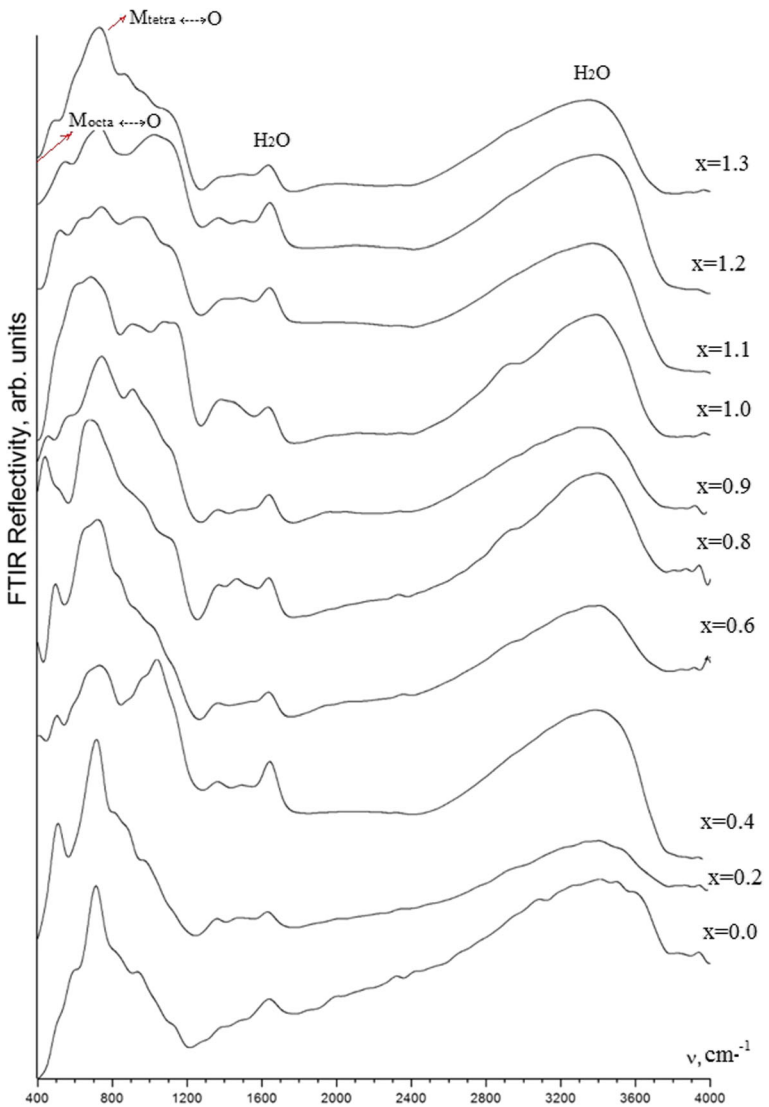

Fig. 8 IR reflection spectra of samples with synthesized pH = 12.5 at different cation ratio

FTIR spectroscopy confirmed the results of magnetic measurements. The decrease in the value of magnetic saturation beginning with $x = 1.0$ is due to the filling of octahedral positions with Mn^{2+} ions.

Abbreviations

CNP: Contact non-equilibrium plasma; DTA: Differential thermal analysis; DTG: Differential thermogravimetric analysis; FTIR: Fourier transform infrared; I_S: Saturation magnetization; SEM: Scanning electron microscopy; T_C: Temperature; TG: Mass loss; XRD: X-ray diffraction; Hc: Coercive force (Oe)

Acknowledgements

The authors are indebted to Mr. A. Baskevich for studying our samples in X-ray diffraction.

Authors' Contributions

LF designed the experiment and drafted the manuscript. LF performed the samples and carried out the experiment. MD helped to analyze and modify the manuscript. All authors read and approved the final manuscript.

Competing Interests

The authors declare that they have no competing interests.

Publisher's Note

Author details

[1]Ukrainian State University of Chemical Technology, Gagarin Ave., 8, Dnipropetrovsk 49005, Ukraine. [2]Oles Honchar Dnipropetrovsk National University, Gagarin Ave., 72, Dnipropetrovsk 49010, Ukraine.

Received: 2 January 2017 Accepted: 7 August 2017
Published online: 23 August 2017

References

1. Forgacs E, Cserhati T, Oros G (2004) Removal of synthetic dyes from wastewaters: a review. Environ Int 30:953–971
2. Hashemian S, Dehghanpor A, Moghahed M (2015) Cu 0.5Mn 0.5Fe2O4 nano spinels as potential sorbent for adsorption of brilliant green. J Ind Eng Chem 24:308–314
3. Deraz N, Shaban S (2009) Optimization of catalytic, surface and magnetic properties of nanocrystalline manganese ferrite. J Anal Appl Pyrolysis 86:173–179
4. Sharma L, Kimura T (2003) FT-IR investigation into the miscible interaction in new materials for optical devices. Polym Adv Technol 14:392–399
5. Gubin SP, Koksharov YA, Khomutov GB et al (2005) Magnetic nanoparticles: preparation, structure and properties. Russ Chem Rev 74:489–518
6. Stolyarchuk IL, Dolgikh LY, Vasilenko IV, Pyatnitskii Yu I, Strizhak PE (2012) Catalysis of steam reforming of ethanol by nanosized manganese ferrite for hydrogen production. Theor Exp Chem 48:129–134
7. Édelman I, Ivanova O, Polyakova K, Polyakov V, Bayukov O (2008) Evolution of the structure and magneto-optical properties of MnxFe3–xO4 films prepared by solid-state reactions. Phys Solid State 50(12):2289–2294
8. Laurent S, Forge D, Port M, Roch A, Robic C, Elst LV, Muller RN (2008) Magnetic iron oxide nanoparticles: synthesis, stabilization, Vectorization, physicochemical characterizations, and biological applications. Chem Rev 108:2064–2110
9. Chen JP, Sorensen CM, Klabunde KJ, Hadjipanayis GC, Devlin E, Kostikas A (1996) Size-dependent magnetic properties of MnFe2O4 fine particles synthesized by coprecipitation. Phys Rev B 54:9288–9296
10. Musat Bujoreanu V, Segal E (2000) On the kinetics of manganese ferrite formation from aqueous solution of MnO2 and FeSO4·7H2O. J Therm Anal Calorim 61:967–977
11. Yang A, Chinnasamy CN, Greneche JM, Chen Y, Yoon SD et al (2009) Large tunability of Néel temperature by growth-rate-induced cation inversion in Mn-ferrite nanoparticles. Appl. Phys Lett 94:113109
12. Pourbafarani S (2014) The effect of alkali concentration on the structural and magnetic properties of Mn-ferrite nanoparticles prepared via the coprecipitation method. Metall and Mat Trans A 45:4535–4538
13. Reddy P, Zhou X, Yann A, Sa D, Huang Q et al (2015) Low temperature hydrothermal synthesis, structural investigation and functional properties of $Co_xMn_{1-x}Fe_2O_4$ ($0 \leq x \leq 1.0$) nanoferrites. Superlattice Microst 81:233–242
14. Misra RDK, Gubbala S, Kale A, Egelhoff WF (2004) A comparison of the magnetic characteristics of nanocrystalline nickel, zinc, and manganese ferrites synthesized by reverse micelle technique. Mat Sci Eng B-Solid 111:164–174
15. Liu C, Zhang ZJ (2001) Size-dependent superparamagnetic properties of Mn spinel ferrite nanoparticles synthesized from reverse micelles. Chem Mater 13:2092–2096
16. Waqas H, Qureshi AH (2009) Influence of pH on nanosized Mn–Zn ferrite synthesized by sol–gel auto combustion process. J Therm Anal Calorim 98:355
17. Solis TV, Vigon PV, Alvarez S, Marban G, Fuertes AB (2007) Manganese ferrite nanoparticles synthesized through a nanocasting route as a highly active Fenton catalyst. Cat Com 8:2037–2042
18. Mahmoud MH, Hamdeh HH, Ho JC, O'Shea MJ, Walker JC (2000) Mossbauer studies of manganese ferrite fine particles processed by ball-milling. J Magn Magn Mater 220(2–3):139–146
19. Muroi M, Street R, McCormick PG, Amighian J (2001) Magnetic properties of ultrafine MnFe2O4 powders prepared by mechanochemical processing. Phys Rev B 63:184414
20. Ding J, McCormick PG, Street R (1997) Formation of spinel Mn-ferrite during mechanical alloying. J Magn Magn Mater 171(3):309–314
21. Mahmouda MH, Williams CM, Cai J, Siu I, Walker JC (2003) Investigation of Mn-ferrite films produced by pulsed laser deposition. J Magn Magn Mater 261:314–318
22. Ju YW, Choi GR, Jung HR, Kim C, Yang KS, Lee WJ (2007) A hydrous ruthenium oxide-carbon nanofibers composite electrodes prepared by electrospinning. J Electrochem Soc 154:A192–A199
23. Kulkarni GU, Kannan KR, Arunarkavalli T, Rao CNR (1994) Particle-size effects on the value of Tc of MnFe2O4: evidence for finite-size scaling. Phys Rev B 49:724–727
24. Deraz NM, El-Shobaky GA (2001) Solid-solid interaction between ferric oxide and manganese carbonate as influenced by lithium oxide doping. Thermochim Acta 375:137–145
25. Frolova LA, Pivovarov AA, Tsepich EG (2016) Non-equilibrium plasma-assisted hydrophase ferritization in Fe^{2+}–Ni^{2+}–$SO4^{2-}$–OH^- System. In: Fesenko O, Yatsenko L (eds) Nanophysics, Nanophotonics, Surface Studies, and Applications, Springer Proceedings in Physics. , Springer, Cham, p.588
26. Guigue-Millot N, Begin-Colin S, Champion Y, Hytch MJ, Le Caer G, Perriat P (2003) Control of grain size and morphologies of nanograined ferrites by adaptation of the synthesis route: mechanosynthesis and soft chemistry. J Solid State Chem 170:30–38
27. Frolova LA, Pivovarov AA (2015) Investigation of conditions for ultrasound-assisted preparation of nickel ferrite. High Energy Chemistry 49(1):10–15
28. Frolova L, Pivovarov A, Tsepich E (2016) Ultrasound ferritization in Fe2+–Ni2+–SO42–OH- system. Journal of Chemical Technology and Metallurgy 51(2):163–167
29. Frolova LA, Pivovarov AA, Baskevich AS (2014) Structure and properties of nickel ferrites produced by glow discharge in the Fe^{2+}–Ni^{2+}–$SO4^{2-}$–OH^- system. Russ J Appl Chem 87(8):1054–1059
30. Bruggeman P et al (2009) Characterization of a direct dc-excited discharge in water by optical emission spectroscopy. Plasma Sources Sci Technol 18(2):025017
31. Choukourov A, Manukyan AS, Shutov DA, Rybkin VV (2016) Physico-chemical properties of dc current discharge plasma with liquid cathode. Izv Vyssh Uchebn Zaved Khim Khim Tekhnol 59(12):4–16
32. Nikiforov A, Xiong Q, Britun N, Snyders R, Lu XP, Leys C (2011) Absolute concentration of OH radicals in atmospheric pressure glow discharges with a liquid electrode measured by laser-induced fluorescence spectroscopy. Appl Phys Expr 4(2):026102
33. Bobkova ES, Rybkin VV (2013) Estimation of electron parameters in the dielectric barrier discharge with a liquid electrode at atmospheric pressure. High Temp 51(6):747–752
34. Gillot B (1994) Infrared spectrometric investigation of submicron metastable cation-deficient spinels in relation to order-disorder phenomena and phase transition. Vib Spectrosc 6:127–148
35. Brabers VAM (1969) Infrared spectra of cubic and tetragonal manganese ferrites. Phys Status Solidi 33:563–572